Meshfree Simulations of Ductile Crack Propagations

Shaofan Li [a] & Cerup B. Simonsen [b]

[a] Department of Civil and Environmental Engineering, University of California, Berkeley, CA,
USA

[b] Department of Mechanical Engineering, Technical University of Denmark, Lyngby, Denmark
Published online: 23 Feb 2007.

PLEASE SCROLL DOWN FOR ARTICLE

Taylor & Francis
Taylor & Francis Group

Meshfree Simulations of Ductile Crack Propagations

Shaofan Li

Department of Civil and Environmental Engineering, University of California, Berkeley CA, USA

Cerup B. Simonsen

Department of Mechanical Engineering, Technical University of Denmark, Lyngby, Denmark

Contents

In this work, a meshfree method is used to simulate ductile crack growth and propagation under finite deformation and large scale yielding conditions. A so-called *parametric visibility condition* and its related particle splitting procedure have been developed to automatically adapt the evolving strong continuity or fracture configuration due to an arbitrary crack growth in ductile materials.

It is shown that the proposed meshfree crack adaption and re-interpolation procedure is versatile in numerical simulations, and it can capture some essential features of ductile fracture and ductile crack surface morphology, such as the rough zig-zag pattern of crack surface and the ductile crack front damage zone, which have been difficult to capture in previous numerical simulations.

1. INTRODUCTION

One of the early incentives to develop meshfree methods is to simulate crack growth and crack propagation (e.g. Belytschko [1994a, b]), because meshfree interpolations have flexibility to adapt the change of the geometry of a solid due to crack growth or fracture, which can be a painful process by using a finite element adaptive process such as remeshing (e.g. Wawrzynek and Ingraffea [1987]).

For two-dimensional elastostatic crack growth, meshfree simulation of crack growth has been a success. Belytschko and his co-workers have systematically applied the so-called element-free Galerkin (EFG) method to simulate crack growth/propagation problems (e.g. Belytschko et al. [1994a, b],[1995a, b], [1996a, b], [1997], Lu et al. [1995], Krysl et al. [1997] and [1999], and Fleming et al. [1997a], among others). Special techniques, such as the visibility criterion, are developed in modeling discontinuous fields in a solid (e.g. Belytschko [1996a] and Krysl

[1997]). Subsequently, other meshfree methods, such as the partition of unity method, the so-called X-finite element method, and the level set method have also been developed and exploited in crack growth simulations (e.g. Daux et al. [2000], Dolbow [2000], Stolarska et al. [2002] and Ventura et al. [2002]). It is fair to say that at least in 2D crack growth simulation meshfree Galerkin procedure offers considerable advantages over the traditional finite element methods, because the global remeshing is avoided.

However, most works published in literature have mainly dealt with elastic crack growth. Few simulation results are reported for inelastic fracture or elastic-plastic crack propagation.

The technical difficulties in simulating inelastic fracture are two: (1) lacking crack growth criterion, and (2) lacking viable numerical algorithms to simulate crack growth without impairing the original interpolation field.

The first difficulty emerges when a ductile fracture is associated with large scale yielding as well as undergoing finite deformation. Under those circumstances, the applicability of J-integral of elastic fracture theory is no longer accurate (see: Xia et al. [1995a, b, c]). The second difficulty is more serious. Because ductile fracture is an irreversible process, the history of state variables, such as plastic strain and yield stress, at each material point, e.g. a Gauss point in a computation domain, have to be preserved in a bookkeeping process at each time step. If the original mesh can not automatically adapt arbitrary crack paths, any remesh process will need the mapping or conversion of state variables from old interpolation field to new interpolation field, which is not only a time-consuming process but also a major source of accumulative numerical error that prohibits any possible accurate long-term simulation.

In computation practice, there are essentially three approaches to simulate ductile fracture: (1) Embed the possible crack path in the original finite element mesh (e.g. Xia et al. [1995a, b]). In the embedded crack path approach, crack can only grow along the element boundary, it usually can not capture the realistic crack path. (2) Use the so-called erosion algorithm (e.g. Rashid [1968]). This is basically a procedure that resets all state variables and mass to zero and nullifies a material point when stress level of the element containing the material point exceeds a certain threshold, which is often referred to as "the killing element procedure." The method is a brute force approach; it is, nevertheless, very efficient in practice. (3) Remesh and remap state variables. At this point, ductile crack remeshing algorithms are essentially academic demonstrations. Long–term simulation seems to be both unreachable and unreasonable.

The objective of this study is to provide a simple but relatively accurate and yet cost-effective solution that may lead to the final solution of this outstanding problem in computational fracture mechanics.

To achieve this objective, we use meshfree interpolation to approximate the discretized fields. We adopt the Gurson-Tvergarrd-Needleman model and a thermal-viscoplastic model in constitutive modeling and in damage assessment. To model surface separation, we use a newly designed parametric visibility condition and its related particle splitting algorithm to modify previous interpolation and connectivity maps among meshfree particles.

The paper is organized in five sections. In Section 2, we first discuss the newly proposed parametric visibility condition, its related particle splitting algorithm, and how to use them in ductile crack surface modeling. The constitutive modeling, numerical formulation are briefly outlined in Section 3. Two numerical examples are presented in Section 4. A few remarks are made in the last section.

2. CRACK SURFACE APPROXIMATION AND VISIBILITY CONDITION

A crucial step to model crack propagation in a numerical simulation is how to represent the evolving crack surface and automatically adjust the interpolation field around the growing crack tip. This process is not only a re-interpolation scheme, but also a process how to model the material re-configuration.

Belytschko and his co-workers (Belytschko et al. [1996]) have developed a so-called visibility condition that can serve as a criterion to automatically adapt the topological connectivity map among meshfree particles.

There are two shortcomings in previous meshfree crack surface representation/visibility condition procedures: (1) crack surface re-construction and representation schemes are complicated. The complexity comes from the searching algorithm and re-interpolation algorithm. Because of the technical complexity, any generalization of meshfree crack surface modeling of three-dimensional fracture or ductile fracture becomes a formidable task; (2) it has been observed that the meshfree shape functions of the re-interpolation field produced by the visibility condition may contain strong discontinuities in meshfree shape functions at certain regions near a crack tip, although we do not know for certain this is indeed a shortcoming.

To simplify the crack surface modeling procedure, we introduce the following crack surface representation and particle splitting algorithm to model crack surface separation.

(a) Crack Surface Representation and Particle Splitting Algorithm

The two-dimensional crack surface is represented by pairs of piece-wise straight lines as shown in Fig. 1. In Fig. 1, the particles on the crack surface are marked as square black boxes, except the crack tip, whereas other meshfree particles are represented as solid circles. In previous meshfree approaches, when a crack grows, the crack surface is being reconstructed by adding new particles. This is not suitable for ductile crack surface modeling, because one has to re-create state variables and re-distribute mass and volume for any newly added particles.

In our approach, a crack tip is always attached to an existing material/interpolation particle. It only moves from one particle to another as shown in Fig. 1.
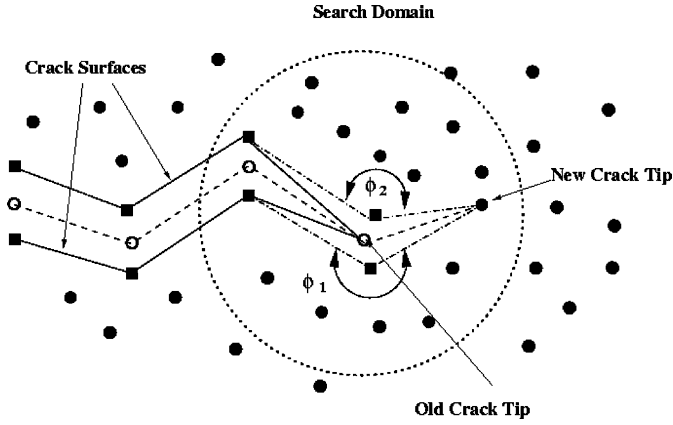
FIG. 1. Illustration of numerical scheme for crack growth.

Assume that the physical criterion to select the new crack tip is available. To find the new crack tip, we first choose a radius R and draw a circle centered at the current crack tip.

Then we apply the crack growth criterion to every point inside the circle to decide which point should be the next crack tip, except those points (square boxes) on the crack surfaces, because we do not allow crack surface to become crack tip again (this may happen in some unusual situations).

Once we selected a new crack tip, we split the old crack tip into two points that have the same value of state variables at that particular time. The mass and volume of the two particles are re-assigned according to the following rules, which are called a particle splitting algorithm:

$$Mass_{new1} = \frac{\phi_1}{2\pi} Mass_{old}, \qquad [2.1]$$

$$Mass_{new2} = \frac{\phi_2}{2\pi} Mass_{old}; \qquad [2.2]$$

and

$$Volume_{new1} = \frac{\phi_1}{2\pi} Volume_{old} \qquad [2.3]$$

$$Volume_{new2} = \frac{\phi_2}{2\pi} Volume_{old} \qquad [2.4]$$

The kinematic field variables, such as displacements, velocity, and accelerations of the new particles are assigned as

$$\mathbf{Disp}_{new1} = \mathbf{Disp}_{old} + \delta \qquad [2.5]$$

$$\mathbf{Disp}_{new2} = \mathbf{Disp}_{old} - \delta \qquad [2.6]$$

$$\mathbf{Vel}_{new1} = \mathbf{Vel}_{old} \qquad [2.7]$$

$$\mathbf{Vel}_{new2} = \mathbf{Vel}_{old} \qquad [2.8]$$

$$\mathbf{Acc}_{new1} = 0.0d0 \qquad [2.9]$$

$$\mathbf{Acc}_{new2} = 0.0d0$$

where δ is a vector whose length $|\delta| \ll 1$. It serves the purpose to make a physical distinction of the two new particles once they are separated.
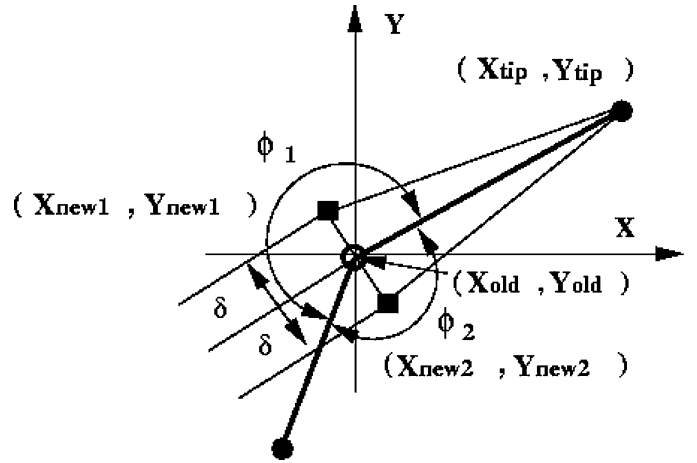
FIG. 2. Meshfree particle splitting algorithm.

This process is illustrated in Fig. 2, in which the point (X_{tip}, Y_{tip}) is the new crack tip, and the old crack tip is split into two particles, (X_{new1}, Y_{new1}) and (X_{new2}, Y_{new2}). A pair of straight lines connect (X_{new1}, Y_{new1}) and (X_{new2}, Y_{new2}) with the new crack tip (X_{tip}, Y_{tip}).

(b) Parametric Visibility Condition

The meshfree interpolation relies on a local connectivity maps to associate one particle with its neighboring particles.

To model crack propagation, one has to develop a numerical algorithm that can automatically modify the local connectivity map and simulate a running crack without user interference.

The following parametric visibility condition is used in the simulation to modify the local meshfree connectivity map to reflect geometric change of domain due to crack growth.

The visibility condition used in this study is illustrated in Fig. 3. Figuratively speaking, a crack may be viewed as an opaque wall. A material point at one side of the wall can not "see" the material points in the other side of the wall. This principle is termed "visibility condition." To determine whether or not two material points are separated by a crack segment, one can

FIG. 3. Visibility condition in 2D.

check whether or not the line segment connecting two material points intercepts the crack path segment.

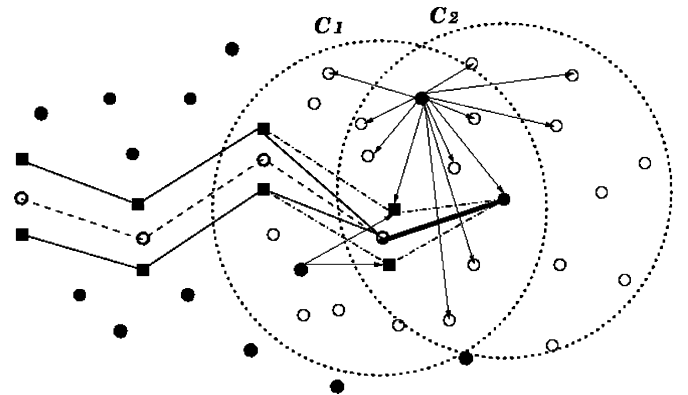Since crack growth is incremental, one only needs to check and to modify a limited number of particles at the current crack tip area, which is defined as the union of two circles centered at the current crack tip and next crack tip (see Fig. 3). To modify the meshfree connectivity map, one only needs to check the visibility condition inside the union of two circles, denoting as $\mathcal{C} = \mathcal{C}_1 \bigcup \mathcal{C}_2$. It is done by a procedure named as "parametric visibility condition."

Suppose that we want modify connectivity relation between particle $(X_{11}, Y_{11}) \in \mathcal{C}$ and the rest of particles inside $\mathcal{C}$. We denote an arbitrary point inside $\mathcal{C}$ as (X_{12}, Y_{12}) and two crack tips (old and new) as (X_{21}, Y_{21}) and (X_{22}, Y_{22}).

The parametric equations of the straight line that connects points (X_{11}, Y_{11}) and (X_{12}, Y_{12}) are

$$\begin{cases} X = X_{11} + \lambda_1 \Delta X_1 \\ Y = Y_{11} + \lambda_1 \Delta Y_1 \end{cases} \qquad [2.10]$$

where λ_1 is the parametric variable and

$$\Delta X_1 := X_{12} - X_{11} \qquad [2.11]$$
$$\Delta Y_1 := Y_{12} - Y_{11} \qquad [2.12]$$

On the other hand, the parametric equation for the straight line that connects two crack tips are

$$\begin{cases} X = X_{21} + \lambda_2 \Delta X_2 \\ Y = Y_{21} + \lambda_2 \Delta Y_2 \end{cases} \qquad [2.13]$$

where λ_2 is the parametric variable and

$$\Delta X_2 := X_{22} - X_{21} \qquad [2.14]$$
$$\Delta Y_2 := Y_{22} - Y_{21} \qquad [2.15]$$

If the two line segments intercept each other, one can equate Eqs. (2.10) and (2.13), and solve for λ_1 and λ_2,

$$\begin{bmatrix} \lambda_1 \\ \lambda_2 \end{bmatrix} = \frac{1}{(\Delta X_1 \Delta Y_2 - \Delta X_2 \Delta Y_1)}$$
$$\times \begin{bmatrix} \Delta Y_2 (X_{21} - X_{11}) - \Delta X_2 (Y_{21} - Y_{11}) \\ \Delta Y_1 (X_{21} - X_{11}) - \Delta X_1 (Y_{21} - Y_{11}) \end{bmatrix} \qquad [2.16]$$

If the two line segments intercept each other, the following **parametric visibility conditions** have to be satisfied,

$$\boxed{0 < \lambda_1 < 1, \text{ and } 0 < \lambda_2 < 1.} \qquad [2.17]$$

These parametric visibility conditions are illustrated in Fig. 4. If both parametric visibility conditions are met, then the line segment between two arbitrary points inside $\mathcal{C}$ will intercept
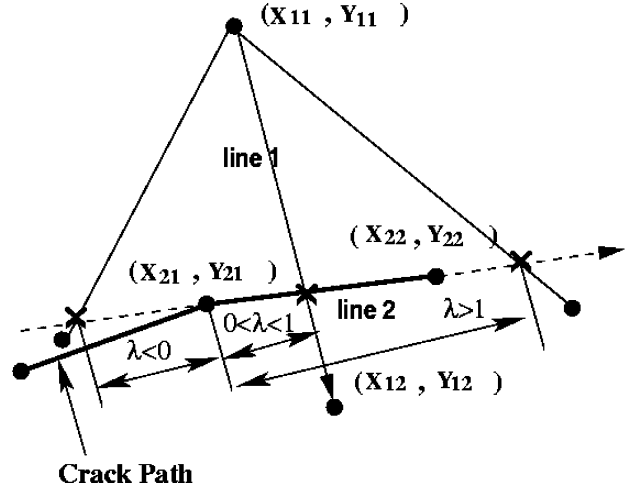

FIG. 4. Parametric visibility conditions.

the newly formed crack surfaces and hence one should disconnect the connections between these two points. In other words, either point should be removed from the other point's connectivity map, and it then ensures that there is no non-physical cross-crack interpolation.

(c) Examples of Meshfree Shape Function Near a Crack Tip

In the following, a few artificial examples are shown to display the meshfree shape functions that are constructed at crack surface via particle splitting algorithm, connectivity modification, and parametric visibility condition.

In Fig. 5(a) and (b), a meshfree shape function is shown whose support has been cut up to 3/4 by two orthogonally running cracks. In Fig. 5(c) and (d), it is shown that a meshfree function has been cut by a crack into two parts and another meshfree shape is right at the crack tip.

A meshfree shape function whose support size has been cut by a crack up to 1/4 is shown in Fig. 6(a) and (b). In Fig. 6(c) and (d), a meshfree shape function has been severed into three different shape functions.

As reported by Belytschko et al. [1996], there are some abnormalities about these meshfree shape functions whose supports have been modified by visibility conditions. One of them is the apparent strong discontinuity at certain locations of the support.

Figure 7 displays the profile of a meshfree shape function right in front of a crack tip. One may observe from Fig. 7(b) that there is discontinuity at the back neck of the shape function. One may wonder why this happens, because based on visibility condition, the support of this meshfree shape function has not changed at all.

As a matter of fact, the visibility condition not only changes the connectivity relations among particles, but also changes the connectivity relations among any material points in the domain
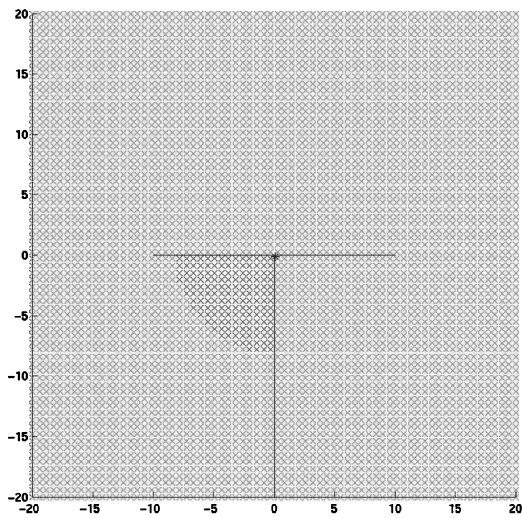
(a)
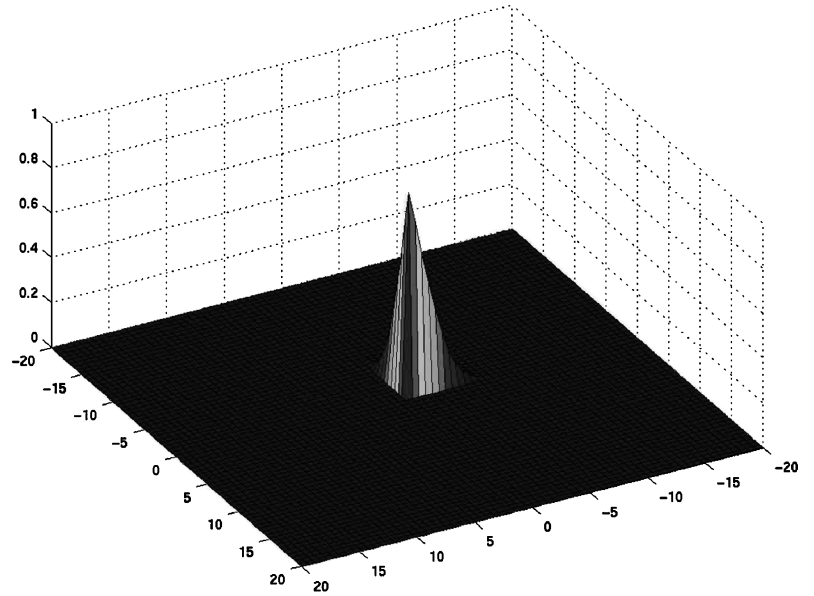
(b)
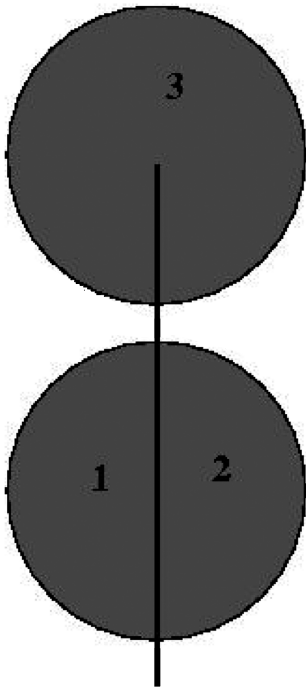
(c)
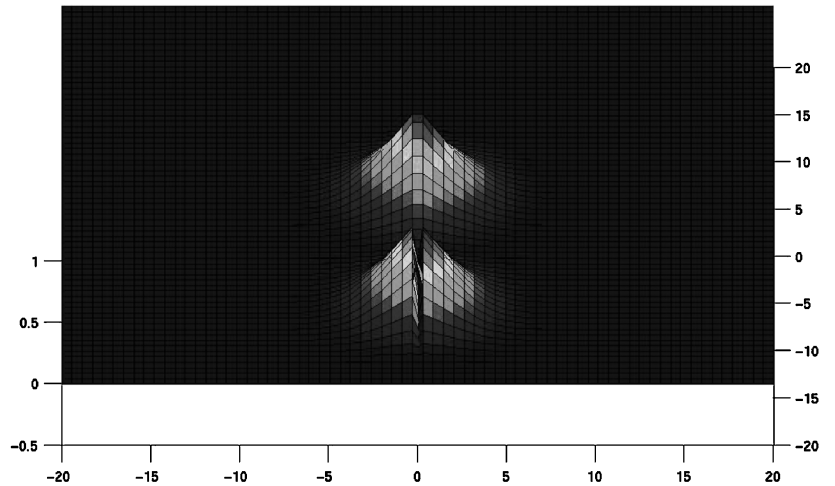
(d)

FIG. 5. Meshfree shape function along crack surfaces (I).

(e.g. Gauss quadrature points) and meshfree particles. More precisely speaking, visibility condition is also used to change the domain of influence of any material point in the neighborhood of a crack. The connective domain of influence for different material points inside the support of the meshfree shape function, where the meshfree shape function is evaluated, has changed. Those changes may not be continuous as a material point moves toward to the crack tip. This situation is illustrated in Fig. 7(c). Shown by Fig. 7(c), as a material point approaches to the crack tip, the domain of influence of a material point suddenly changes

(a)

(b)

(c)

(d)
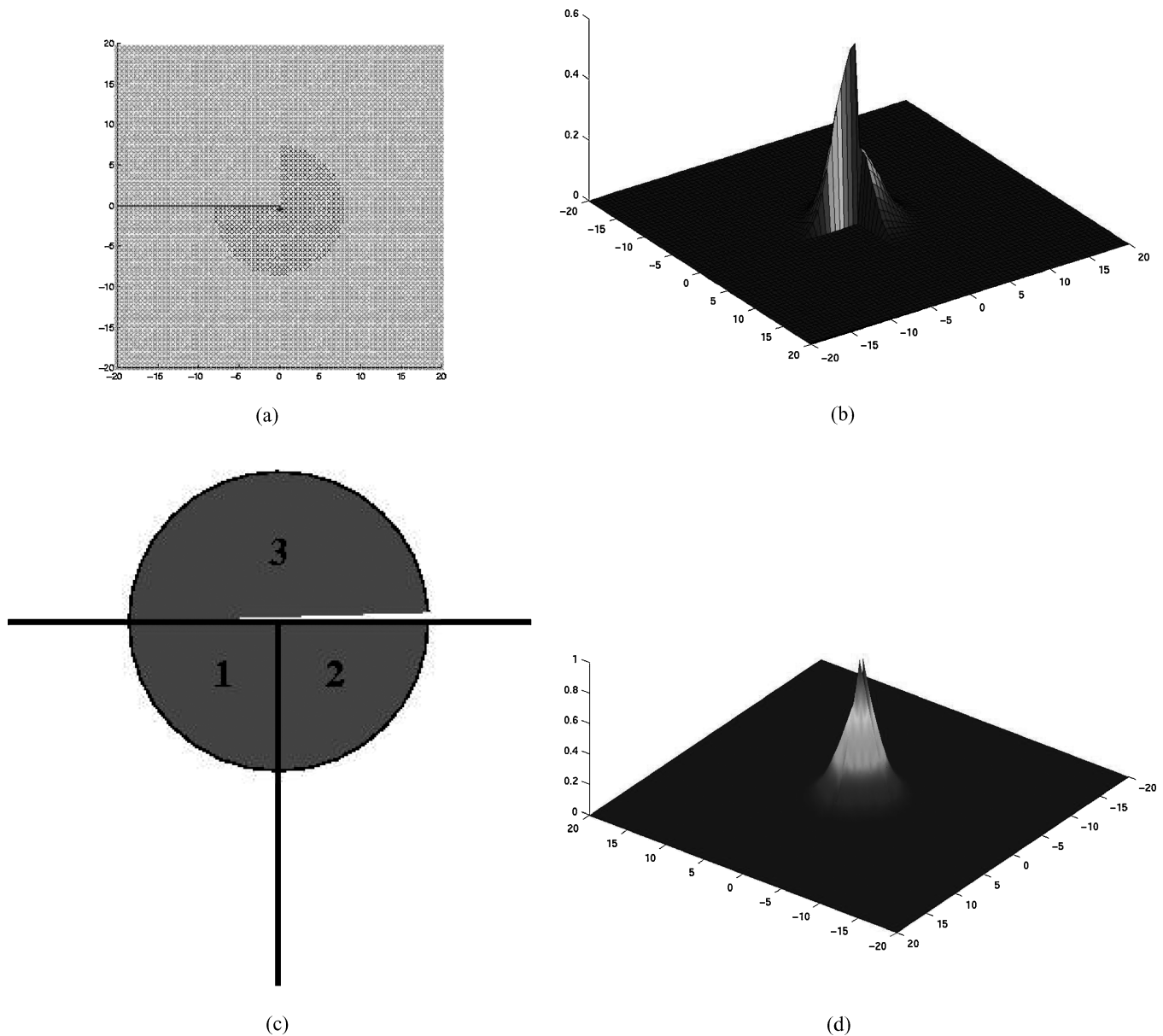
FIG. 6.   Meshfree shape function along crack surfaces (II).

from a half circle to 3/4 of a circle, and with a slight move towards the right or down, the domain of influence of a material point will become almost a full circle except the crack line. This sudden change of domain of influence is the source of strong discontinuity that appears in the profile of the meshfree shape function.

Some believed that such discontinuity in the meshfree shape function may affect the performance of meshfree shape functions and hence affect the accuracy of the crack tip interpolation field. In fact, Belytschko and his co-workers were developing other methods, for instance the so-called diffraction method, to avoid having discontinuous meshfree shape functions near the crack tip region.

Nonetheless, no definitive evidence has been found to link the discontinuity of meshfree shape function with poor interpolation accuracy. It is still an open question to assess the effect of such discontinuity of meshfree shape functions, since the completeness of meshfree interpolation near the crack tip is not affected by such discontinuity. Therefore, in our numerical simulations, close to a crack tip the meshfree shape function with discontinuity is used without any further modifications.

3. CONSTITUTIVE MODELINGS

In this work, we consider fracture of inelastic solids undergoing finite deformations. For inelastic large deformations, the

(a)

(b)

Sudden Change of Domain of Influence

Support I

(c)
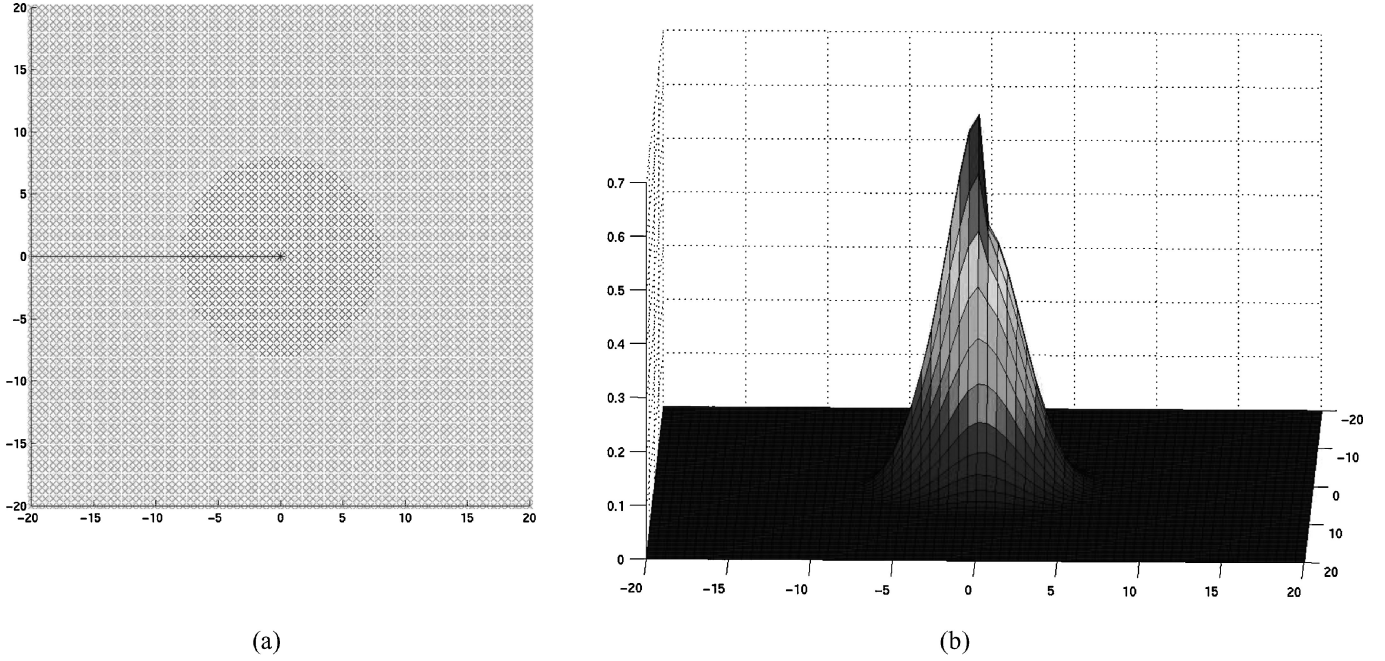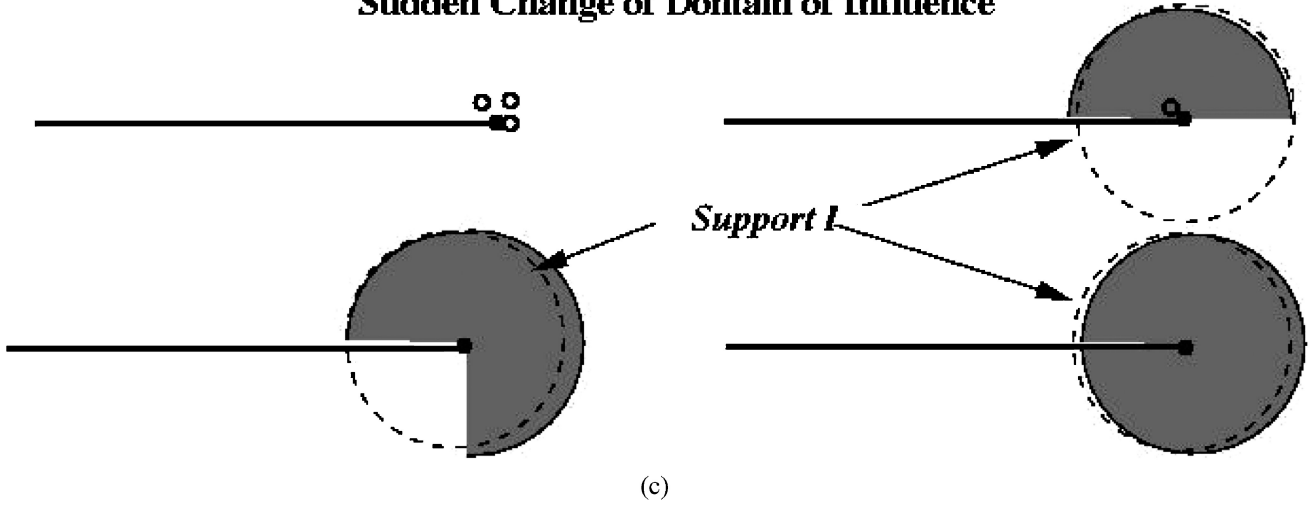
FIG. 7. Strong discontinuity of a meshfree shape function at a crack tip.

deformation gradient, **F**, may be decomposed as

$$\mathbf{F} = \mathbf{F}^e \cdot \mathbf{F}^{ine} \qquad [3.1]$$

where $\mathbf{F}^e$ describes elastic deformations and rigid body rotations, and $\mathbf{F}^{ine}$ represents inelastic deformations. The rate of deformation tensor, **D**, and the spin tensor, **W**, are the symmetric and anti-symmetric parts of the spatial velocity gradient $\mathbf{L} = \dot{\mathbf{F}} \cdot \mathbf{F}^{-1}$, i.e.

$$\mathbf{D} + \mathbf{W} = \dot{\mathbf{F}} \cdot \mathbf{F}^{-1} = \dot{\mathbf{F}}^e \cdot \mathbf{F}^{e-1} + \mathbf{F}^e \cdot \dot{\mathbf{F}}^{ine} \cdot \mathbf{F}^{ine-1} \cdot \mathbf{F}^{e-1} \qquad [3.2]$$

and

$$\mathbf{D} := D_{ij}\mathbf{e}_i \otimes \mathbf{e}_j , \quad D_{ij} := \frac{1}{2}\left(\frac{\partial v_i}{\partial x_j} + \frac{\partial v_j}{\partial x_i}\right) \qquad [3.3]$$

$$\mathbf{W} := W_{ij}\mathbf{e}_i \otimes \mathbf{e}_j , \quad W_{ij} := \frac{1}{2}\left(\frac{\partial v_i}{\partial x_j} - \frac{\partial v_j}{\partial x_i}\right) \qquad [3.4]$$

where v_i are the velocity components.

Two inelastic constitutive relations have been used in our numerical simulations: (1) The Gurson-Tvergaard-Needleman (GTN) model and (2) a thermo-viscoplastic material.

(a) Gurson-Tvergaard-Needleman Model

Consider the rate form constitutive model. The rate-of-deformation tensor $\mathbf{D}$ is decomposed into additive elastic and plastic parts,

$$\mathbf{D} = \mathbf{D}^{el} + \mathbf{D}^{pl} \qquad [3.5]$$

The Jaumann rate of the Cauchy stress is used in hypoelastic formulation, i.e.

$$\boldsymbol{\sigma}^{\nabla J} = \mathbf{C} : \mathbf{D}^{el} = \mathbf{C} : (\mathbf{D} - \mathbf{D}^{pl}) \qquad [3.6]$$

where the Jaumann rate is defined as

$$\boldsymbol{\sigma}^{\nabla J} := \dot{\boldsymbol{\sigma}} - \mathbf{W} \cdot \boldsymbol{\sigma} + \boldsymbol{\sigma} \cdot \mathbf{W}, \qquad [3.7]$$

where $\{\dot{\ }\} = \frac{d}{dt}\{\}$, and the elastic tensor is isotropic,

$$C_{ijk\ell} = \left(K - \frac{2}{3}G\right)\delta_{ij}\delta_{k\ell} + G(\delta_{ik}\delta_{j\ell} + \delta_{i\ell}\delta_{jk}) \qquad [3.8]$$

the bulk and shear moduli can be linked to the Young's modulus and Poisson's ratio by

$$G = \frac{E}{2(1+\nu)} \qquad [3.9]$$

$$K = \frac{E}{3(1-2\nu)} \qquad [3.10]$$

Define the hydrostatic, deviatoric, and equivalent stresses as

$$\sigma_m = \frac{1}{3}\boldsymbol{\sigma} : \mathbf{I}^{(2)} \qquad [3.11]$$

$$\mathbf{s} = \boldsymbol{\sigma} - \sigma_m \mathbf{I}^{(2)} \qquad [3.12]$$

$$\sigma_{eq} = \left(\frac{3}{2}\mathbf{s} : \mathbf{s}\right)^{1/2} \qquad [3.13]$$

The plastic rate of deformation is obtained from the following flow rule,

$$\mathbf{D}^{pl} = \dot{\lambda}\frac{\partial \Phi}{\partial \boldsymbol{\sigma}} = \dot{\lambda}\left(\frac{1}{3}\frac{\partial \Phi}{\partial \sigma_m}\mathbf{I}^{(2)} + \frac{\partial \Phi}{\partial \sigma_{eq}}\mathbf{n}\right) \qquad [3.14]$$

where

$$\mathbf{n} := \frac{3}{2\sigma_{eq}}\mathbf{s} \qquad [3.15]$$

and the yield potential is defined as

$$\Phi = \left(\frac{\sigma_{eq}}{\sigma_0}\right)^2 + 2q_1 f^*(f)\cosh\left(\frac{3q_2\sigma_m}{2\sigma_0}\right)$$
$$- \left(1 + q_1^2(f^*(f))^2\right) = 0. \qquad [3.16]$$

In Eq. (3.16), parameters q_1 and q_2 were introduced by Tvergaard [1982], [1990] to bring predictions of the original Gurson model

(Gurson [1972]) into a closer agreement with numerical analysis of a periodic array of voids. The volume fraction of void is characterized by the following function (Tvergaard and Needleman [1984]),

$$f^*(f) = \begin{cases} f, & \forall\, f \le f_c \\ f_c + \dfrac{1/q_1 - f_c}{f_f - f_c}(f - f_c), & \forall\, f_c < f \le f_f \\ 1/q_1, & \forall\, f > f_f \end{cases}$$
$$\qquad [3.17]$$

where f_c is the volume fraction of void at onset of coalescence and f_f is the final volume fraction of void. Equation (3.17) takes into account both effects of void growth and coalescence.

In (3.16), if $f^*(f) = 0$, the plastic yield potential reduces to von Mises potential of J_2 flow theory. The void volume growth rate is due to both void expansion and and new void nucleation,

$$\dot{f} = \dot{f}_{growth} + \dot{f}_{nucleation} \qquad [3.18]$$

For incompressible materials, the growth rate of the existing void is,

$$\dot{f}_{growth} = (1 - f)\mathbf{D}^{pl} : \mathbf{I}^{(2)} \qquad [3.19]$$

whereas the void nucleation rate is assumed to be

$$\dot{f}_{nucleation} = \frac{f_N \dot{\bar{\epsilon}}^{pl}}{s_N\sqrt{2\pi}}\exp\left[-\frac{1}{2}\left(\frac{\bar{\epsilon}^{pl} - \epsilon_N}{s_N}\right)^2\right] \qquad [3.20]$$

where f_N is the volume of void nucleating particles, ϵ_N is the mean value strain, and s_N is the standard deviation for strain distribution.

The plastic strain rate is determined by

$$\dot{\bar{\epsilon}}^{pl} = \frac{\boldsymbol{\sigma} : \mathbf{D}^{pl}}{(1 - f)\sigma_0} \qquad [3.21]$$

and the yield stress obeys a power law,

$$\bar{\sigma}_0 = \sigma_Y \left(1 - \frac{E}{\sigma_Y}\bar{\epsilon}^{pl}\right)^N \qquad [3.22]$$

where σ_Y is the initial yield stress, E is Young's modulus, $\bar{\epsilon}^{pl}$ is the effective plastic strain, and N is the power index.

Detailed information on numerical integration and constitutive update of GTN model can be found in Aravas [1987] and Simonson and Li [2004].

(b) Thermo-Elasto-Viscoplastic Model

The second constitutive model used in the fracture test is a thermo-elasto-viscoplastic solid (see Zhou, Ravichandran, and Rosakis [1996b] for details).

The the rate form constitutive equation is

$$\boldsymbol{\sigma}^{\nabla J} := \mathbf{C} : (\mathbf{D} - \mathbf{D}^{vp} - \mathbf{D}^t), \qquad [3.23]$$

where the thermal rate of deformation, $\mathbf{D}^t$, is given as

$$\mathbf{D}^t = \alpha \dot{T} \mathbf{I}^{(2)} \qquad [3.24]$$

here α is the coefficient of thermal expansion, and the coupled viscoplastic deformation rate is described by,

$$D_{ij}^{vp} := \bar{\eta}(\bar{\sigma}, \bar{\epsilon}, T) \frac{\partial \Phi}{\partial \sigma_{ij}} \qquad [3.25]$$

$$\bar{\eta} = \dot{\epsilon}_0 \left[\frac{\bar{\sigma}}{g(\bar{\epsilon}, T)} \right]^m, \qquad [3.26]$$

$$g(\bar{\epsilon}, T) = \sigma_0 [1 + \bar{\epsilon}/\epsilon_0]^N \left\{ 1 - \delta \left[\exp\left(\frac{T - T_0}{\kappa} \right) - 1 \right] \right\} \qquad [3.27]$$

where both m and N are power indices, $\dot{\epsilon}_0$ is the referential strain rate, σ_0 is yield stress, $\epsilon_0 = \sigma_0/E$, T_0 is the room temperature, and both κ and δ are thermal softening parameters. In Eqs. 3.25–3.27, the effective plastic strain is defined as

$$\bar{\epsilon} := \int_0^t \sqrt{\frac{2}{3} \mathbf{D}^{vp} : \mathbf{D}^{vp}} \, dt \qquad [3.28]$$

and the yield potential of viscoplastic solid is of the von Mises type,

$$\Phi(\sigma_{eq}, \sigma_0) = \left(\frac{\sigma_{eq}}{\sigma_0} \right)^2 - 1 \qquad [3.29]$$

For detailed discussion, one may consult a paper by Zhou et al. [1996].

The local form of the energy equation is

$$\rho_0 C_p \frac{\partial T}{\partial t} = \chi \boldsymbol{\tau} : \mathbf{D}^{vp} + \nabla_{\mathbf{X}}(J\mathbf{F}^{-1} \cdot \mathbf{K} \cdot \mathbf{F}^{-T} \cdot \nabla_{\mathbf{X}} T), \quad \forall \mathbf{X} \in \Omega_0 \qquad [3.30]$$

where $\mathbf{K}$ is the heat conductivity tensor, χ is the fraction of plastic work converted to heat, and C_p is the specific heat capacity.

Considering fast crack propagation, we neglect the effect of heat conduction. Under the condition of adiabatic heating, we have

$$\rho_0 C_p \frac{\partial T}{\partial t} = \chi \boldsymbol{\sigma} : \mathbf{D}^{vp} \qquad [3.31]$$

4. MESHFREE SIMULATIONS

The ensuing meshfree simulation is based on the following total Lagrangian variational (weak) formulation,

$$\int_{\Omega_X} \rho_0 \ddot{u}_i \delta u_i d\Omega_X + \int_{\Omega_X} P_{Ji} \delta F_{Ji}^T d\Omega_X$$
$$- \int_{\Omega_X} \rho_0 B_i \delta u_i d\Omega_X - \int_{\Gamma_X^T} T_i^0 \delta u_i d\Gamma = 0 \qquad [4.1]$$

where T_i^0 is the components of prescribed traction force on the traction boundary, Γ_X^T, and $\mathbf{P}$ denotes the nominal stress tensor, which is the transpose of the first Piola-Kirchhoff stress, and it can be related to the Cauchy stress tensor by the expression, $\boldsymbol{\sigma} = J^{-1}\mathbf{F} \cdot \mathbf{P}$, ρ_0 is the density in referential configuration, and $\mathbf{B} = B_i \mathbf{e}_i$ is the body force per unit mass.

The boundary conditions in referential configuration are

$$\mathbf{n} \cdot \mathbf{P} = \mathbf{T}^0, \quad \forall \mathbf{X} \in \Gamma_X^T \qquad [4.2]$$

$$\mathbf{u} = \bar{\mathbf{u}}, \quad \forall \mathbf{X} \in \Gamma_X^u \qquad [4.3]$$

It should be noted that the meshfree interpolant used is not able to represent boundary data via boundary value interpolation. Therefore, an extra term appears in the weak form (4.1)

$$\int_{\Gamma_X^u} \mathbf{T}^0 \cdot \delta \mathbf{u} d\Gamma_X \qquad [4.4]$$

because $\delta \mathbf{u} \neq \mathbf{0}$, $\forall \mathbf{X} \in \Gamma_X^u$. On how to estimate this term and enforce the essential conditions, the readers may be referred to Li and Liu [2000].

Assume that the trial and weighting functions have the same form of interpolation,

$$\mathbf{u}^h(\mathbf{X}, t) = \sum_{I=1}^{NP} N_I(\mathbf{X}) \mathbf{d}_I(t) \qquad [4.5]$$

$$\delta \mathbf{u}^h(\mathbf{X}, t) = \sum_{I=1}^{NP} N_I(\mathbf{X}) \delta \mathbf{d}_I(t) \qquad [4.6]$$

where NP is the total number of particles.

The weak form (4.1) will yield the following discrete equation

$$\mathbf{M}\ddot{\mathbf{d}} + \mathbf{f}^{int} = \mathbf{f}^{ext} \qquad [4.7]$$

where $\mathbf{M}$ is the mass matrix, and

$$\mathbf{f}_I^{ext} = \int_{\Gamma_X^T} T_i^0(X, t) N_I(X) \mathbf{e}_i d\Gamma$$
$$+ \int_{\Omega_X} B_i(X, t) N_I(X) \mathbf{e}_i d\Omega \qquad [4.8]$$

$$\mathbf{f}_I^{int} = \int_{\Omega_X} P_{Ji} \frac{\partial N_I}{\partial X_J} \mathbf{e}_i d\Omega \qquad [4.9]$$

V = 10 m/s, 20 m/s, or 30 m/s

2 mm or 20 mm

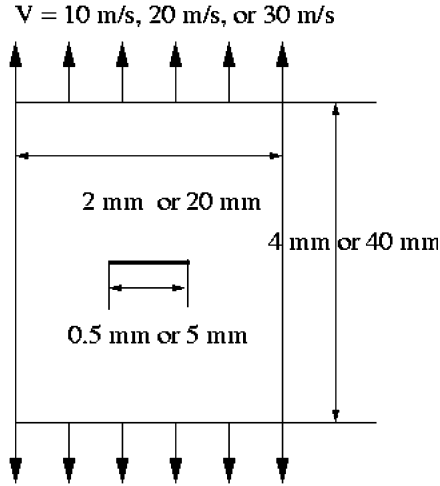4 mm or 40 mm

0.5 mm or 5 mm

FIG. 8. Dimensions of the tension test specimens.

(a) Example I: Gurson-Tvergaard-Needleman Model

In the first example, we simulate ductile fracture of a thin plate (see Fig. 8).

As shown in Fig. 8, the rectangular specimen has a center crack embedded in the middle of the plate, which has the initial length, 0.5 mm. Velocity boundary conditions are prescribed at both ends of the plate, so it renders the plate under uniaxial tension loading.

The GTN model is used in the first example. The following material parameters are used,

$$E = 211 \text{ GPa}$$
$$\rho = 7800 \text{ kg m}^3$$
$$\nu = 0.3$$
$$\sigma_Y = 469 \text{ MPa} \qquad [4.10]$$
$$q_1 = 1.5, \quad q_2 = 1.0, \quad q_3 = 2.25, \quad f_0 = 0.0025,$$
$$f_N = 0.02, \quad f_c = 0.15, \quad f_f = 0.25;$$
$$\epsilon_N = 0.3, \quad s_N = 0.1. \qquad [4.11]$$

The fracture criteria that we used is a damage based criterion. Initially, we set up a critical damage value as fracture threshold. In this example, that threshold is chosen as $f_{cr} = 0.12$. At each time step, we evaluate damage value of each particle in the neighborhood of the crack tip (the circle in Fig. 1). Once the damage value of a particle exceeds f_{cr}, we declare the particle as the new crack tip. If damage values of two and more particles exceed f_{cr} at the same time step, there may be the sign to signal crack bifurcation.

In the current simulation, we simply choose the particle that has largest damage value among all the other particles whose damage values exceed f_c as the new crack tip.

Zooming in the crack region, we can observe crack surface morphology. Fig. 11 shows stress distribution, σ_{22}, around a crack region. It is a close snap-shot of crack configurations at two different time instances.

A careful observation of Fig. 11 reveals some important features of ductile fracture. First, there is a growing blue region that indicates a growing region with small normal stress value, which is an indication of the growth of the traction-free crack surfaces. This fact proves that the crack surfaces constructed by automatically adjusting meshfree interpolation field are indeed traction-free, $\sigma_{22} = 0$, and it provides the right physics around the propagating crack tip. Second, the ductile crack surface shows a zig-zag pattern. This zig-zag pattern of rough crack surface that is the trademark of ductile fracture (see Xia et al. [1995a,b,c]). To the best of the authors' knowledge, such unique a feature of ductile fracture has been difficult to capture in previous numerical simulations. Third, visible necking due to strain softening and material instability can be found Figs. 9, 10, and 11.

To test the size-effect, a second numerical simulation is conducted with a larger specimen, 20 mm × 40 mm. The size of the tension specimen is ten times larger than the specimen used in the first simulation, and the length of the initial center crack is 5 mm long. The prescribed velocity is also increased to 30 m/s.

The contours of normal stress, σ_{22}, and damage distribution are depicted in Fig. 12. As may be observed in Fig. 12, the crack path is not perpendicular to the tension direction as happened in the first simulation. After initial crack growth, the crack paths then follow an inclined angle ($40° \sim 50°$) through the specimen. This suggests that for this particular geometry of the specimen, the ductility of the specimen increases when its size increases.

(b) Example II: Thermo-Elasto-Viscoplastic Model

In the second numerical example, the tension test specimen (Fig. 8) is assumed to be made of a thermo-elasto-viscoplastic material (See Zhu et al. [1996b]). The dimension of the plate is 20 mm × 40 mm, and the initial length of the crack is 5 mm. In the numerical experiment, the prescribed tension velocity is chosen as 20 m/s. The actual material parameters used in the simulation are tabulated in Table 1.

The fracture criterion for the thermo-elasto-viscoplastic material can be chosen either based on the maximum tensile stress (hoop stress) criterion or based on a critical effective strain criterion. In the particular example reported in this paper, the critical effective strain criterion is used.

In the process of selecting a new crack tip, we measure the effective strain at each point in a circle surrounding the crack tip. An empirical strain value is chosen as the critical effective strain ($\epsilon_{cr} = 0.15$). When the effective strain of a particle inside the circle surrounding the crack tip reaches to the critical effective strain, we declare that point the new crack tip. Once the new crack tip is determined, one can connect the new crack tip with the old crack tip in a straight line, which depends on the coordinates of new crack tip and old crack tip.

Once the linear equation of the line segment connecting the old and the new crack tips is established, one can apply the proposed parametric visibility condition to modify the connectivity
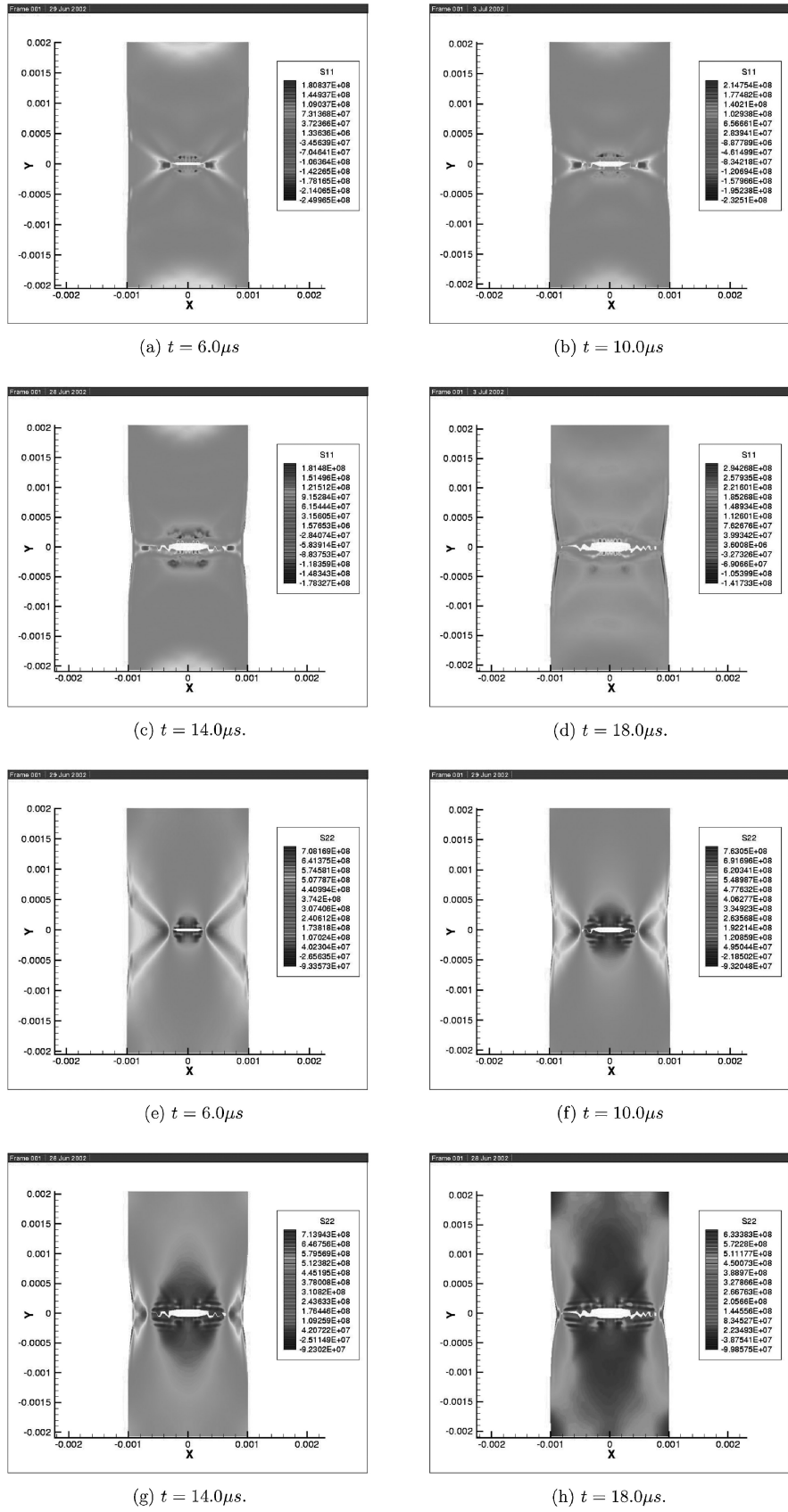
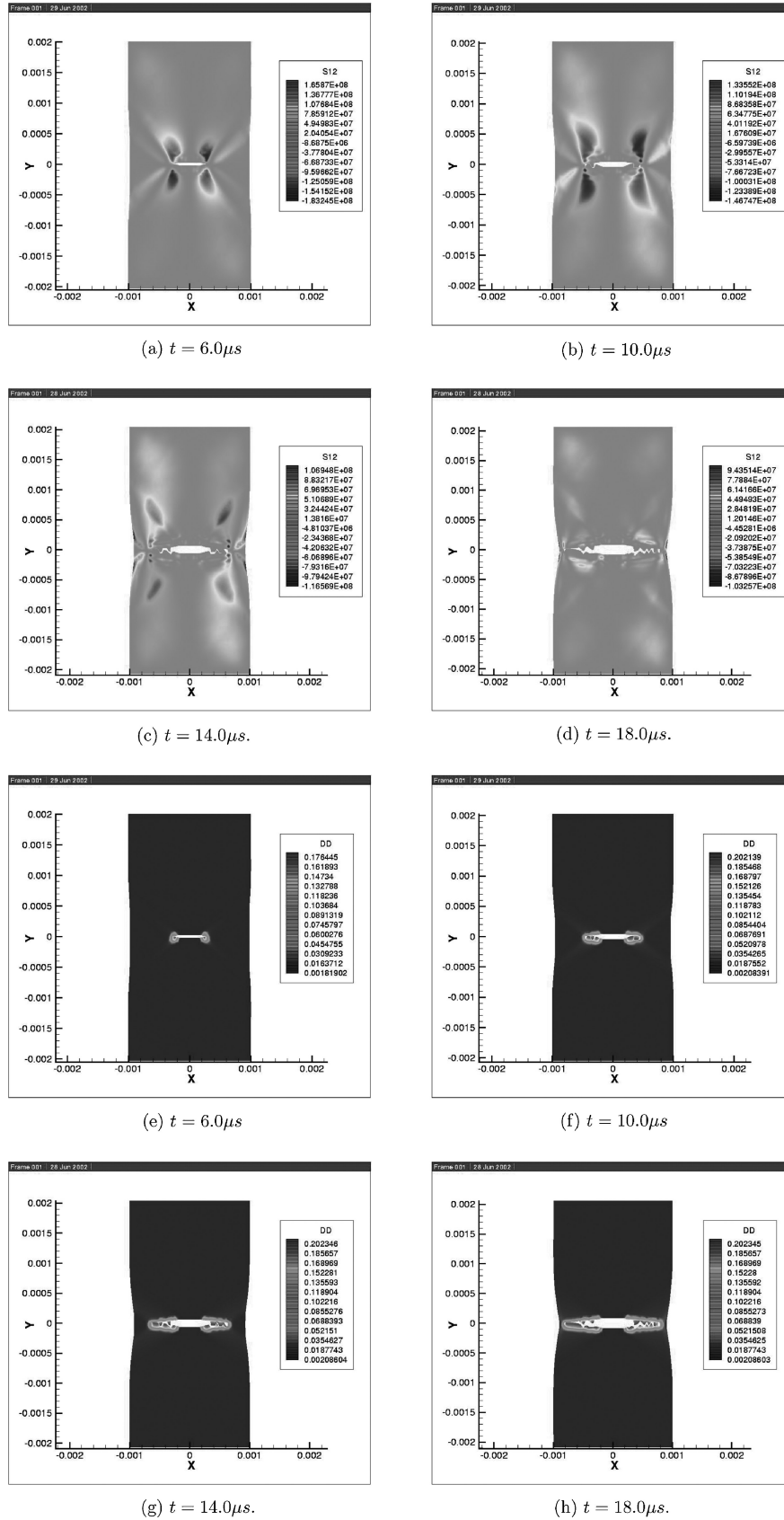**FIG. 9.** The stress contours: σ_{11} (a), (b), (c), (d) and σ_{22} (e), (f), (g), and (h).

(a) $t = 6.0\mu s$

(b) $t = 10.0\mu s$

(c) $t = 14.0\mu s$.

(d) $t = 18.0\mu s$.

(e) $t = 6.0\mu s$

(f) $t = 10.0\mu s$

(g) $t = 14.0\mu s$.

(h) $t = 18.0\mu s$.

FIG. 10.   Shear stress σ_{12} contours (a), (b), (c), (d) and damage distribution (e), (f), (g), and (h).

(a) $t = 10.0\mu s$ (b) $t = 14.0\mu s$

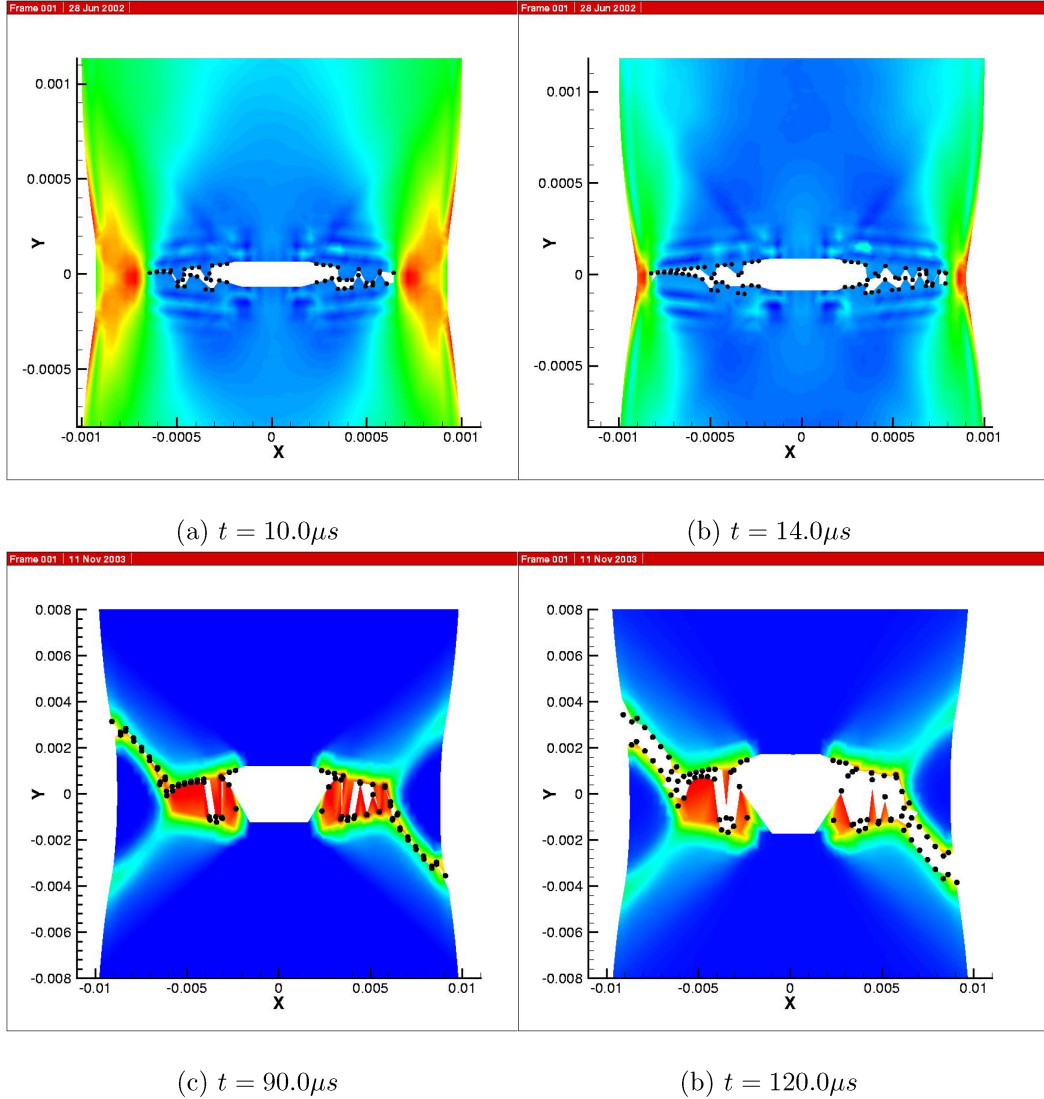(c) $t = 90.0\mu s$ (b) $t = 120.0\mu s$

FIG. 11. Crack surface morphology: σ_{22} contour for the small specimen (a) and (b), damage f contour for the large specimen (c) and (d).

map and hence to construct the new and traction-free crack surface.

In the numerical example reported, the critical effective strain is chosen as $\epsilon_{cr} = 0.15$ and the other material properties of the thermal-viscoplastic material are listed in Table 1.

In Fig. 13, the stresses components, σ_{12} and σ_{22}, are displayed at various time instances during the fast crack propagation process. Since the critical effective strain criterion is used to grow crack, the crack path takes an almost a $45°$ angle with the horizontal line. This is because that the maximum effective strain occurs at the direction that forms almost $45°$ angle with the remote vertical direction loading, whereas in GTN model, the maximum damage always occurs ahead of the crack tip almost horizontally.

It is interesting to note that in Fig. 13(a), (b), (c), and (d), one can find that across the growing crack surfaces, shear stress,

σ_{12}, changes its sign. This is shown by the fact that there is a blue region (lower shear stress value) below the crack surface, and there is a red region (higher shear stress value) above the crack surface. First, this fact again verifies that the crack surface constructed by meshfree interpolation is indeed traction free, i.e. both normal stress and shear stress are zero across the crack surface. Second, this fact shows the feature of a local mixed mode fracture. Third, from Fig. 14, one can observe the temperature induced thermal-softening and its consequence: strain localization. Adiabatic shear bands can be observed from both temperature profile as well as effective strain rate profile.

All the numerical experiments reported in this paper have the same center crack geometry, which may not be the best configuration to study ductile fracture. Nonetheless, the main focus of this paper is the crack growth algorithm rather than the physical features or mechanisms of ductile fracture, which has been
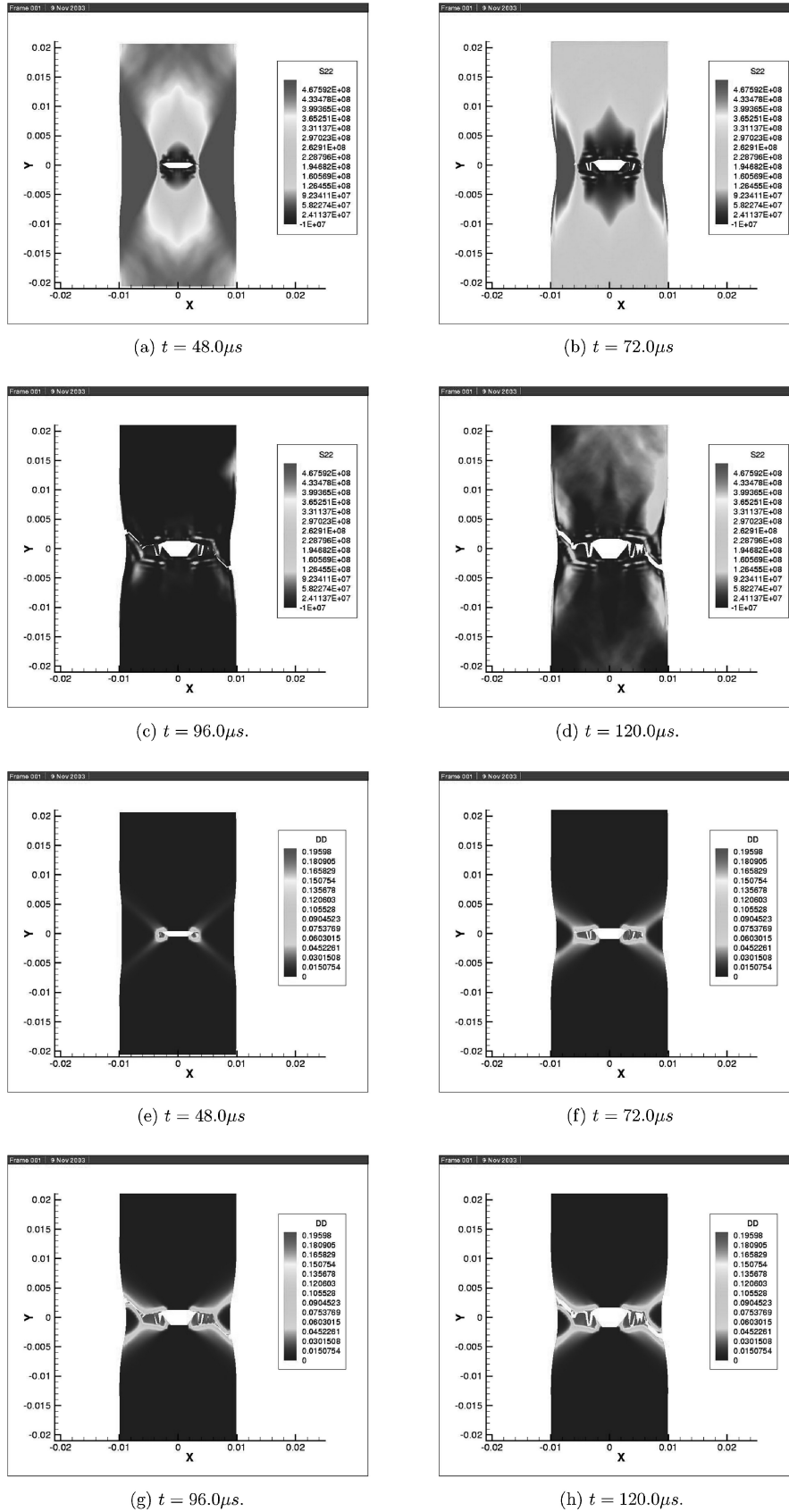
(a) $t = 48.0\mu s$

(b) $t = 72.0\mu s$

(c) $t = 96.0\mu s$.

(d) $t = 120.0\mu s$.

(e) $t = 48.0\mu s$

(f) $t = 72.0\mu s$

(g) $t = 96.0\mu s$.

(h) $t = 120.0\mu s$.

FIG. 12. The contours of normal stress σ_{22}: (a), (b), (c), (d) and damage distribution: (e), (f), (g), (h).

TABLE 1
Material parameters used in the computer simulations

Parameter	Value	Definition
$\dot{\epsilon}_0$	$1 \times 10^{-3} \mathrm{s}^{-1}$	Reference strain rate
m	70	Rate sensitivity parameter
σ_0	200 MPa	Yield stress
ϵ_0	σ_0/E	
N	0.01	Strain hardening exponent
T_0	293 K	Reference temperature
δ	0.8	Thermal softening parameter
κ	500 K	Thermal softening parameter
E	200 GPa	Young's modulus
ν	0.3	Poisson's ratio
ρ_0	7830 kg m^{-3}	Mass density
C_p	448 J (kg $\cdot$ K)$^{-1}$	Specific heat
α	11.2×10^{-6} K^{-1}	Coefficient of thermal expansion
χ	0.9	The fraction of plastic work converted to heat
$\dot{\epsilon}_r$	4.0×10^4 1/s	In a range $(1.0 \times 10^4$ 1/s $\sim 6.0 \times 10^4$ 1/s$)$

the main subject of an article by the same authors (Simonsen and Li [2004]). In that paper, a more realistic three-point bending test is simulated by using the proposed crack growth algorithm, and the numerical results are compared with experimental data.

5. DISCUSSIONS

There are a few important technical issues worth discussing.

First, there have been regularized versions of the Gurson model proposed (e.g. Pan and Huang [1994]); however, the digital version of a regularized Gurson model is still developing. The GTN model used in this simulation is the standard version used in numerical computations, which has been extensively used in research to study ductile failures; recent works include: Pardoen and Hutchinson [2000], Benzerga [2002], Becker [2002], and Besson and Guillemer-Neel [2003]. The boundary-value problems involved with the GTN model are not completely ill-posed, since plastic dissipation due to the damage is considered in the numerical computation. Damage or void growth introduces a length scale in the current formulation used. Because this length scale is very small, strong mesh dependency and mesh sensitivity are expected in finite element simulations. One of the advantages of combining meshfree methods with GTN model to simulate ductile fracture is that the meshfree interpolation may provide a numerical smoothing effect or regularization effect. This is because that the meshfree interpolation is a non-local interpolation, and it tends to smooth out or to smear the high gradient displacement field or even discontinuous field caused by strain localization. Even though this effect strongly depends on meshfree particle distribution, but it is very helpful because the conventional GTN model may not be well regularized, though damage-induced plastic dissipation has been taken into account in the current simulation.

Second, by using meshfree simulation alone, one can not eliminate mesh sensitivity, in this case, the particle distribution dependency. To a certain extent, the numerical results presented in this paper may alter when different particle distributions are employed. Nevertheless, the authors believed that the main features captured in this study will remain, such as the zig-zag crack surface morphology. In fact, the initial particle distribution used in the simulation is almost uniform throughout the domain. They are placed in a square pattern and they are symmetric based on the mesh generator's precision, which may introduce a small random error distribution for the particle distribution considered.

The asymmetric fracture pattern obtained in simulations can be attributed to the following factors: (1) The simulation is based on the explicit computation. In each time step, fracture criterion is being checked within a circle in front of the corresponding crack tip. Once an old crack tip moves to its new position, new crack surfaces are constructed, new particles are created due particle splitting algorithm, and the crack tip field is re-interpolated. In explicit computations, individual crack growth is simulated in the order of initial numbering. This may result in an asymmetric interaction between cracks, which, in fact, is a reflection of reality. (2) Ductile fracture is involved with material instabilities, and there are quite a few bifurcation modes in front of a crack tip, which are extremely sensitive to small perturbations. A slight perturbation in round-off error or slight variation on random error distribution of particle positions will cause one bifurcation mode active and suppress the other bifurcation modes. Since the machine precision perturbation is random in time and particle position error is random in space, one should expect different crack growth patterns for different cracks, though overall symmetric or anti-symmetric patterns can still be observed in the simulations. This is again a reflection of the reality of ductile fracture, because the randomness of numerical error may mimic the randomness spatial inhomogeneities.
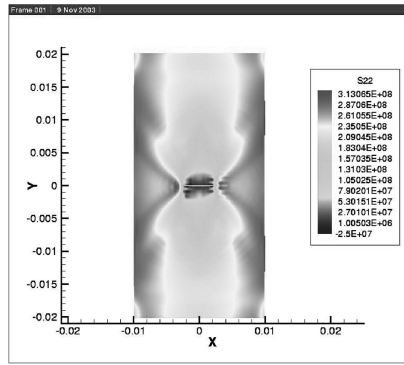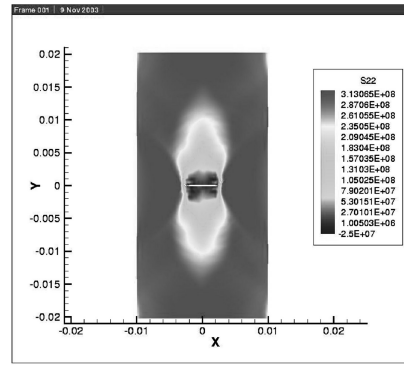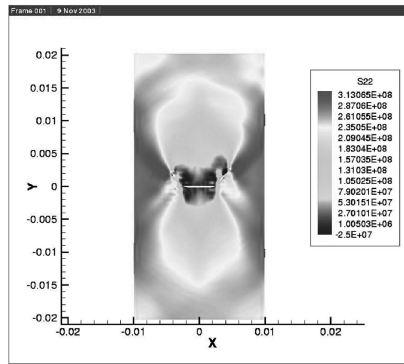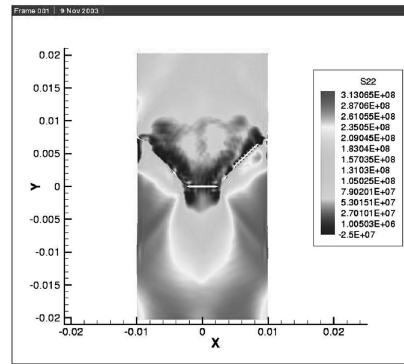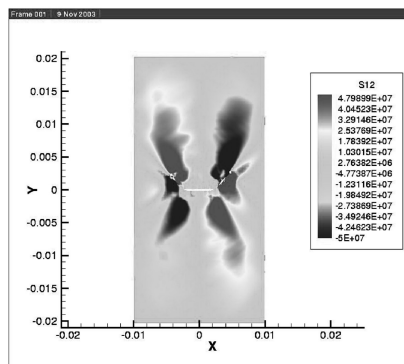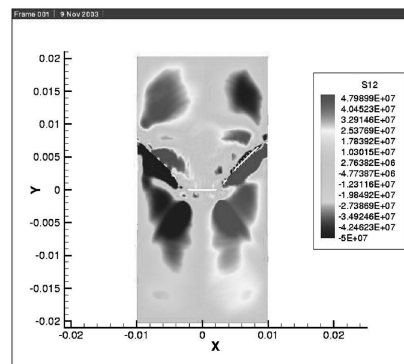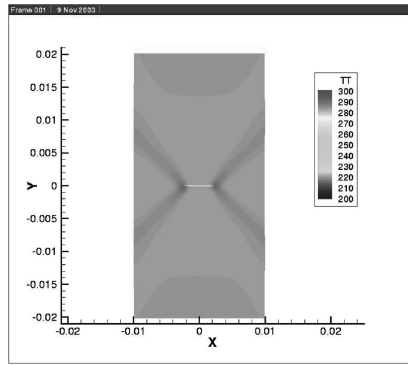
(a) $t = 16.0\mu s$

(b) $t = 20.0\mu s$

(c) $t = 24.0\mu s$
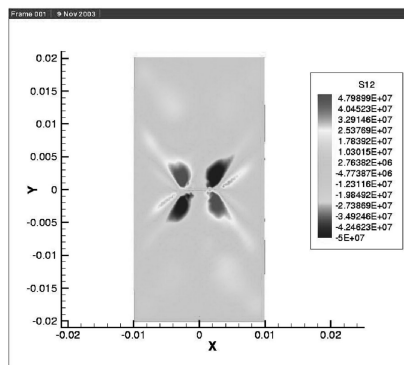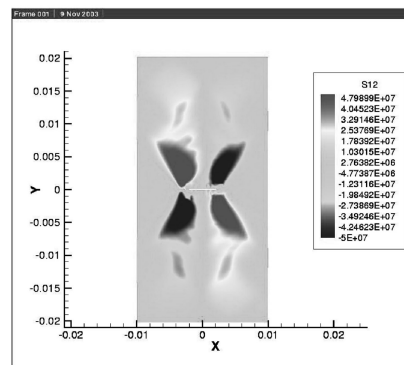
(d) $t = 28.0\mu s$

(e) $t = 16.0\mu s$

(f) $t = 20.0\mu s$

(g) $t = 24.0\mu s$.

(h) $t = 28.0\mu s$.

FIG. 13. Stress contours: σ_{22} (a), (b), (c), (d) and σ_{12} (e), (f), (g), (h).
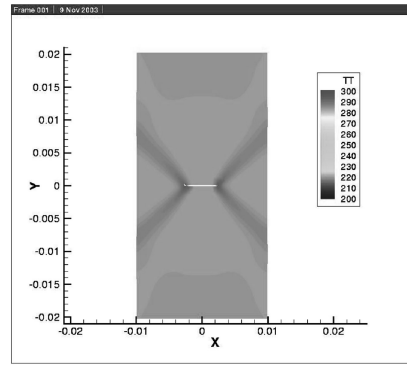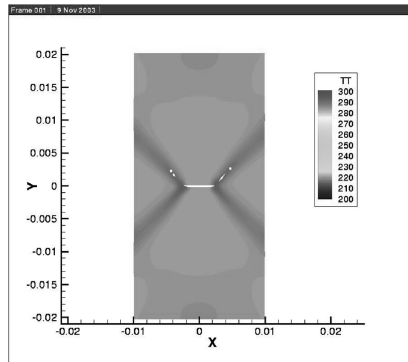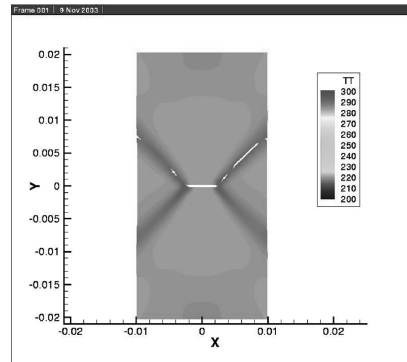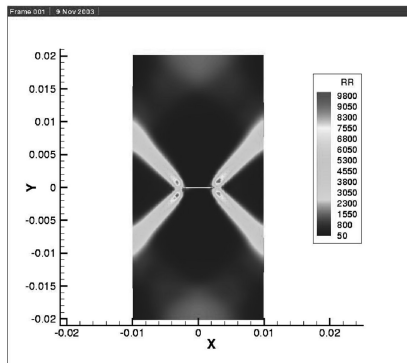
(a) $t = 16.0\mu s$
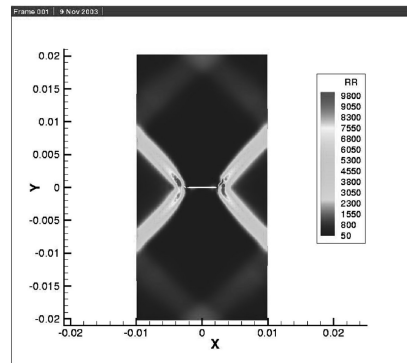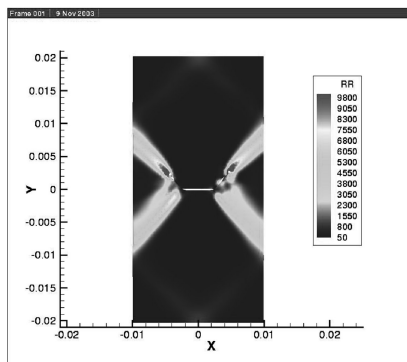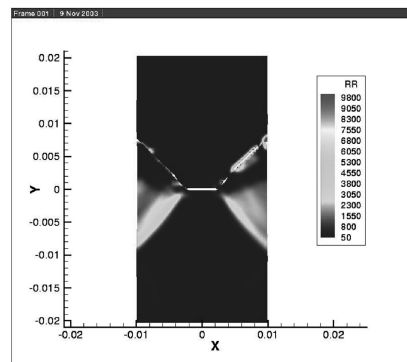

(b) $t = 20.0\mu s$

(c) $t = 24.0\mu s$.

(d) $t = 28.0\mu s$.

(e) $t = 16.0\mu s$

(f) $t = 20.0\mu s$

(g) $t = 24.0\mu s$.

(h) $t = 28.0\mu s$.

FIG. 14. Temperature contours (a), (b), (c), (d) and effective strain rate contours (e), (f), (g), (h).

The micromechanics of void growth and its damage introduces an intrinsic length scale. Physically, this is the dimension of representative volume element. When the length of the particle spacing approaches this scale, one should expect the convergence of numerical computations, though this has not been demonstrated in this paper.

6. CONCLUSION

In this work, we have developed a novel meshfree interpolation procedure to adaptively re-construct ductile crack surfaces with different fracture criteria. The numerical computations show that the proposed procedure can accurately simulate crack growth and propagation in ductile materials undergoing finite deformation and large scale yielding.

This work's contributions to computational fracture mechanics and meshfree methods include: (1) the new parametric visibility condition; (2) the new particle splitting algorithm; and (3) its ability to describe inelastic solids with evolving discontinuity and its ability to adapt finite deformation and large scale yielding.

Moreover, the proposed meshfree procedures are simple, robust, and efficient, which can be easily extended to three-dimensional (3D) simulations, and it can be used to simulate ductile crack propagation in three dimensional objects.

REFERENCES

Aravas, N., "On the numerical integration of a class of pressure-dependent plasticity models," *International Journal for Numerical Methods in Engineering* **24**, 1395–1416 (1987).

Becker, R., "Ring fragmentation predictions using the Gurson model with material stability conditions as failure criteria," *International Journal of Solids and Structures* **39**, 3555–3580 (2002).

Belytschko, T., Lu, Y. Y., and Gu, L., "Element free galerkin methods," *International Journal for Numerical Methods in Engineering* **37**, 229–256 (1994a).

Belytschko, T., Lu, Y. Y., and Gu, L., "Fracture and crack growth by element-free Galerkin methods," *Model. Simul. Sci. Comput. Engrg.* **2**, 519–534 (1994b).

Belytschko, T., Lu, Y. Y., and Gu, L., "Element-free galerkin methods for static and dynamic fracture," *International Journal of Solids and Structures* **32**, 2547–2570 (1995a).

Belytschko, T., Lu, Y. Y., and Gu, L., "Crack propagation by Element-free Galerkin Methods," *Engineering Fracture Mechanics* **51**, 295–315 (1995b).

Belytschko, T., Krongauz, Y., Organ, D., Fleming, M., and Krysl, P., "Meshless methods: An overview and recent developments," *Computer Methods in Applied Mechanics and Engineering* **139**, 3–48 (1996a).

Belytschko, T., Krongauz, Y., Fleming, M., Organ, D., and Liu, W.K., "Smoothing and accelerated computations in the element free Galerkin method," *Journal of Computational and Applied Mathematics* **74**, 111–126 (1996b).

Belytschko, T., and Tabbara, M., "Dynamic fracture using element-free galerkin methods," *Journal of Computational and Applied Mathematics* **39**, 923–938 (1997).

Benzerga, A. A., "Micromechanics of coalescence in ductile fracture," *Journal of the Mechanics and Physics of Solids* **50**, 1331–1362 (2002).

Besson, J., and Guillemer-Neel, C., "An extension of the Green and Gurson models to kinematic hardening," *Mechanics of Materials* **8**, 1–18 (2003).

Daux, C., Moes, N., Dolbow, J., Sukumar, N., and Belytschko, T., "Arbitrary branched and intersecting cracks with the extended finite element method," *International Journal for Numerical Methods* **48**, 1741–1760 (2000).

Dolbow, J., Moës, N., and Belytschko, T., "Discontinuous enrichment in finite elements with a partition of unity method," *Finite Elements in Analysis and Design* **36**, 235–260 (2000).

Fleming, M., Chu, Y. A., Moran, B., Belytschko, T., "Enriched element-free Galerkin methods for crack tip fields," *International Journal for Numerical Methods in Engineering* **40**, 1483–1504 (1997).

Gurson, A. L., "Continuum theory of ductile rupture by void nucleation and growth: Part I yield criteria and flow rules for porous ductile materials," *Journal of Engineering Materials and Technology* **99**, 2–15 (1977).

Krajcinovi, D., *Damage Mechanics*, Elsevier, Amsterdam (1996).

Krysl, P., and Belytschko, T., "Element-free Galerkin method: convergence of the continuous and discontinuous shape function," *Computer Methods in Applied Mechanics and Engineering* **148**, 257–277 (1996).

Krysl, P., and Belytschko, T., "The element free Galerkin method for dynamic propagation of arbitrary 3-D cracks," *International Journal of Solids and Structures* **44**, 767–800 (1999).

Li, S., and Liu, W. K., "Numerical simulations of strain localization in inelastic solids using Meshfree methods," *International Journal of Numerical Methods for Engineering* **48**, 1285–1309 (2000).

Lu, Y. Y., Belytschko, T., and Tabbara, M., "Element-free Galerkin method for wave Propagation and dynamic fracture," *Computer Methods in Applied Mechanics and Engineering* **126**, 131–153 (1995).

McClintock, F. A., "A criterion for ductile fracture by the growth of holes," *ASME Journal of Applied Mechanics* **35**, 363–371 (1968).

Pan, K. L., and Huang, Z. P., "A cylindrical void growth model in visco-plastic materials," *International Journal of Damage Mechanics* **3**, 87–106 (1994).

Pardoen, T., and Hutchinson, J. W., "An extended model for void growth and coalescence," *Journal of the Mechanics and Physics of Solids* **48**, 2467–2512 (2000).

Rashid, Y. R., "Analysis of prestressed concrete vessels," *Nuclear Engineering Design* **7**, 334–355 (1968).

Simonsen, B. C., and Li, S., "Meshfree modeling of ductile fracture," Accepted for publication in *International Journal of Numerical Methods for Engineering* **60**, 1425–1450 (2004).

Stolarska, M., Chopp, D.L., Moes, N., and Belytschko, T., "Modelling crack growth by level sets in the extended finite element method," *International Journal of Numerical Methods for Engineering* **51**, 943–960 (2001).

Tvergaard, V., "Influence of voids on shear band instabilities under plane strain conditions," *International Journal of Fracture* **17**, 389–407 (1981).

Tvergaard, V., "On localization in ductile materials containing voids," *International Journal of Fracture* **18**, 237–251 (1982).

Tvergaard, V., and Needleman, A., "Analysis of the cup-cone fracture in a round tensile bar," *Acta Metallurgica* **32**, 157–169 (1984).

Tvergaard, V., "Material failure by void growth to coalescence," *Advances in Applied Mechanics* **27**, 83–151, Edited by Hutchinson, J. W. & Wu, T. Y. Academic Press, New York (1990).

Ventura, G., Xu, J. X., and Belytschko, T., "A vector level set method and new discontinuity approximations for crack growth by EFG," *International Journal for Numerical Methods in Engineering* **54**, 923–944 (2002).

Wawrzynek, P. A., and Ingraffea, A. R., "Interactive finite element analysis of fracture processes: an integrated approach," *Theoretical and Applied Fracture Mechanics* **8**, 137–150 (1987).

Xia, L., Shih, C. F., and Hutchinson, J. W., "Computational approach to ductile crack growth under large scale yielding conditions," *Journal of Mechanics and Physics of Solids* **43**, 389–413 (1995a).

Xia, L., and Shih, C. F., "Ductile crack growth –II. Void nucleation and geometry effects on macroscopic fracture behavior," *Journal of Mechanics and Physics of Solids* **43**, 1953–1981 (1995b).

Xia, L., Shih, C. F., and Hutchinson, "A computational approach to ductile crack growth under large scale yielding conditions," *Journal of Mechanics and Physics of Solids* **43**, 389–413 (1995c).

Zhou, M., Rosakis, A. J., and Ravichandran, G., "Dynamically propagating shear bands in impact-loaded prenotched plates—I. experimental investigations of temperature signatures and propagation speed," *Journal of Mechanics of Physics and Solids* **44**, 981–1006 (1996a).

Zhou, M., Ravichandran, G., and Rosakis, A. J., "Dynamically propagating shear bands in impact-loaded prenotched plates—II. numerical simulations," *Journal of Mechanics of Physics and Solids* **44**, 1007–1032 (1996b).